



Delft University of Technology

Experimental Investigation of Over-the-Wing Propeller–Boundary-Layer Interaction

de Vries, R.; van Arnhem, N.; Avallone, F.; Ragni, D.; Vos, Roelof; Eitelberg, G.; Veldhuis, L.L.M.

DOI

[10.2514/1.J059770](https://doi.org/10.2514/1.J059770)

Publication date

2021

Document Version

Final published version

Published in

AIAA Journal: devoted to aerospace research and development

Citation (APA)

de Vries, R., van Arnhem, N., Avallone, F., Ragni, D., Vos, R., Eitelberg, G., & Veldhuis, L. L. M. (2021). Experimental Investigation of Over-the-Wing Propeller–Boundary-Layer Interaction. *AIAA Journal: devoted to aerospace research and development*, 59(6), 2169–2182. <https://doi.org/10.2514/1.J059770>

Important note

To cite this publication, please use the final published version (if applicable).
Please check the document version above.

Copyright

Other than for strictly personal use, it is not permitted to download, forward or distribute the text or part of it, without the consent of the author(s) and/or copyright holder(s), unless the work is under an open content license such as Creative Commons.

Takedown policy

Please contact us and provide details if you believe this document breaches copyrights.
We will remove access to the work immediately and investigate your claim.



Experimental Investigation of Over-the-Wing Propeller–Boundary-Layer Interaction

Reynard de Vries,* Nando van Arnhem,[†] Francesco Avallone,[‡] Daniele Ragni,[§] Roelof Vos,[¶]
Georg Eitelberg,^{**} and Leo L. M. Veldhuis^{**}

Delft University of Technology, 2629 HS Delft, The Netherlands

<https://doi.org/10.2514/1.J059770>

This experimental study focuses on the aerodynamic interaction between an over-the-wing (OTW) propeller and a wing boundary layer. An OTW propeller is positioned above the hinge line of a wing with a trailing-edge flap. Measurements are carried out with and without axial pressure gradients by deflecting the flap and by extending the flat upper surface of the wing in the streamwise direction, respectively. Surface-pressure taps, microphones, and particle image velocimetry are combined to quantify both the time-averaged and unsteady interaction effects. Results show that the propeller generates an adverse pressure gradient on the wing surface that scales linearly with thrust and decreases with increasing blade-tip clearance. The pressure gradient is partially caused by slipstream contraction, which decelerates the flow near the wall. Additionally, the surface-pressure fluctuations generated beneath the propeller blades and slipstream are stronger than the time-averaged pressure increase due to flow deceleration. Consequently, the propeller triggers flow separation over the hinge line when the flap is deflected. A parametric study of different propeller locations indicates that increasing the tip clearance is not an effective way to mitigate flow separation. However, displacing the propeller half a radius upstream of the hinge line creates a Coandă effect, which allows the flow to remain attached.

Nomenclature

C_p	= pressure coefficient; $(p - p_\infty)/q_\infty$
$C_{p,t}$	= total-pressure coefficient; $(p_t - p_{t,\infty})/q_\infty + 1$
C_T	= thrust coefficient; $T/(\rho_\infty n^2 D^4)$
c	= wing chord, m
c_l	= sectional lift coefficient
D	= diameter, m
f	= frequency, Hz
J	= advance ratio; $V_\infty/(nD)$
M	= Mach number
n	= rotational speed, Hz
p	= static pressure, Pa
p_t	= total pressure, Pa
q_∞	= freestream dynamic pressure; $0.5\rho_\infty V_\infty^2$, Pa
R	= radius, m
Re	= Reynolds number
T	= thrust, N
u, v, w	= Cartesian velocity components, m/s
V	= velocity magnitude, m/s
W	= weighting function
X, Y, Z	= Cartesian coordinates, m
α	= angle of attack, deg; or vortex velocity ratio
β	= blade pitch angle, deg

Γ	= circulation, m^2/s
δ_f	= flap-deflection angle, deg
δ_{99}	= boundary-layer thickness, m
ϵ	= tip clearance, m
μ	= dynamic viscosity, $Pa \cdot s$
ρ	= density, kg/m^3
ϕ	= blade phase angle, deg
ω	= vorticity, 1/s
ω^*	= normalized vorticity; $\omega D/u_{eff}$

Subscripts

c	= wing-chord based
eff	= effective
FP	= flat plate
ind	= induced
off	= propeller off
on	= propeller on
p	= propeller
q	= query location
tip	= blade tip
vx	= vortex
0.7	= at 70% of the blade radius
∞	= freestream quantity

Superscripts

\sim	= phase-averaged component
$'$	= unsteady component

I. Introduction

Presented as Paper 2019-3035 at the AIAA Aviation 2019 Forum, Dallas, TX, June 17–21, 2019; received 7 May 2020; revision received 30 October 2020; accepted for publication 10 November 2020; published online 15 March 2021. Copyright © 2021 by the authors. Published by the American Institute of Aeronautics and Astronautics, Inc., with permission. All requests for copying and permission to reprint should be submitted to CCC at www.copyright.com; employ the eISSN 1533-385X to initiate your request. See also AIAA Rights and Permissions www.aiaa.org/randp.

*Ph.D. Candidate, Flight Performance and Propulsion Section, Faculty of Aerospace Engineering, South Holland; R.deVries@tudelft.nl. Member AIAA.

[†]Ph.D. Candidate, Flight Performance and Propulsion Section, Faculty of Aerospace Engineering, South Holland. Member AIAA.

[‡]Assistant Professor, Aeroacoustics Section, Faculty of Aerospace Engineering, South Holland. Member AIAA.

[§]Associate Professor, Aeroacoustics Section, Faculty of Aerospace Engineering, South Holland. Member AIAA.

[¶]Assistant Professor, Flight Performance and Propulsion Section, Faculty of Aerospace Engineering, South Holland. Associate Fellow AIAA.

^{**}Full Professor, Flight Performance and Propulsion Section, Faculty of Aerospace Engineering, South Holland. Member AIAA.

TO MEET the expected growth in air traffic while limiting the environmental impact of the aviation industry, aircraft configurations with novel propulsion systems are required [1,2]. Throughout the last decade, numerous studies have identified hybrid-electric propulsion as an enabling technology for more efficiently integrated propulsion systems [3–8]. An example of such propulsion systems is the over-the-wing (OTW) propeller. Over-the-wing propellers can significantly increase the lift-to-drag ratio of the wing [9–12] and reduce flyover noise [13,14]. Similar benefits are obtained when the propeller is lowered into a “channel-wing” configuration [9,15]. Nevertheless, several drawbacks have limited the use of OTW propellers. These include a reduced propulsive efficiency when

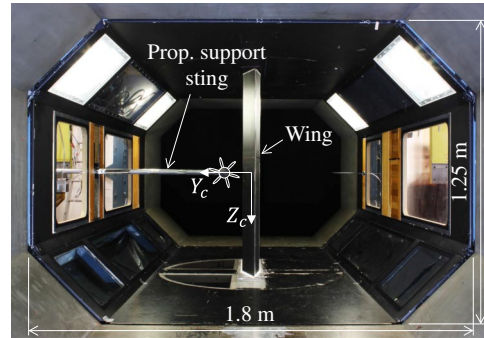
compared to tractor propellers [9,16], an increased nosedown thrust-induced pitching moment, and the need for large support pylons. However, the flexibility of electrical motors allows the propulsive power to be divided over multiple adjacent OTW propellers without compromising the specific weight or efficiency of the motors, thus reducing the diameter of each propulsor while maintaining an equivalent disk loading. This layout, known as over-the-wing distributed propulsion [17], can partially mitigate the penalties associated with large OTW propellers [18] and, additionally, enables short takeoff and landing operations when installed on a flap [19]. As a consequence, several studies focusing on the aerodynamic characteristics of an array of small propellers or fans placed over the wing have been performed in recent years [20–22].

Earlier studies show that it is possible to estimate the aeropropulsive performance of OTW propellers in cruise conditions using panel methods [18] or Reynolds-averaged Navier–Stokes (RANS) simulations [23]. However, predicting the high-lift performance of these systems is a difficult challenge, despite its decisive influence on the sizing process of distributed-propulsion aircraft [24]. The work of Müller et al. [25] has shown that steady RANS simulations are insufficient to accurately predict the aerodynamic interaction between an OTW propeller and the wing when the flap is deflected. The authors identified the unsteady interaction between the propeller tip vortices and the wing boundary layer as a possible cause of flow separation over the flap, which was not captured in steady analyses. Both theoretical [26] and experimental [27] studies have shown that vortex/boundary-layer interaction significantly affects the displacement thickness of the boundary layer, and that it can indeed lead to local flow separation [28,29]. It is also known that a convecting vortex produces pressure fluctuations on the wall surface and increases the turbulent kinetic energy in the boundary layer [30]. Even in the inviscid limit, a rectilinear vortex convected parallel to a wall can lead to reverse flow, depending on the ratio between the self-induced vortex speed and the uniform flow speed [31].

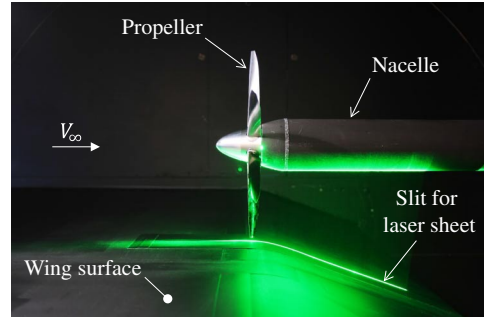
These vortex/boundary-layer interaction studies do not consider the presence of a rotor close to the wall, which imposes additional pressure gradients and three-dimensional effects. The experiments of Murray et al. [32] show that, in that case, flow reversal can occur locally beneath the rotor and that additional unsteady vortical structures are formed, which are comparable to the ground-vortex effect on propeller aircraft [33] or propeller-hull interaction effects in marine applications [34,35]. Moreover, if the tip clearance between the rotor and the wall is small, the local thrust increases not only due to the local reduction in inflow velocity, but also due to the end-plate effect [36]. This leads to local variations in blade loading [25] and tip-vortex strength [37]—contrary to ducted rotors, where the tip vortices (if present) can persist inside the boundary layer without azimuthal variations [38].

Additional complications arise when the propeller is positioned above a wing. In that case, the wing curvature introduces an additional streamwise pressure gradient in the boundary layer, which changes its receptivity to the perturbations of the propeller. Moreover, the inflow conditions to the propeller disk are altered, in terms of both velocity magnitude and angle of attack. This leads to a variation in the loading distribution across the entire disk [23], and causes the slipstream to deform [18]. It is therefore unclear how the interaction between the propeller blades and the wing boundary layer affects flow separation, especially when an additional pressure gradient is generated by the flap.

The objective of this paper is therefore to characterize the steady and unsteady aerodynamic interaction effects that occur between an OTW propeller and the boundary layer of a wing. Due to the difficulty of modeling this unsteady, three-dimensional, viscous problem numerically without validation data, an experimental approach is considered necessary as a first step. The test matrix and wing model of the experiment are designed specifically to meet this objective rather than to obtain an accurate estimation of OTW system performance, which is not the purpose of this study. Measurements are performed with a two-dimensional wing featuring a trailing-edge flap and in a quasi-flat-plate configuration in order to identify how the interaction with the boundary layer is affected by an external pressure gradient. Furthermore, different thrust settings, boundary-layer thicknesses, tip clearances, and axial positions of the propeller are



a) Test section (viewed from behind)



b) Close-up of propeller (viewed from below)

Fig. 1 Overview of wind-tunnel setup, showing position of wing model and installation of propeller (Prop.) relative to the wing.

analyzed in order to establish the impact of each of these parameters on the aerodynamic interaction phenomena. A single propeller is used in this study to isolate these phenomena from the additional ones that would appear if multiple adjacent propulsors were considered. The wing and propeller models are described in Sec. II along with the employed measurement techniques, whereas the characteristics of the isolated wing are given in Sec. III. A detailed description of the time-averaged and unsteady aerodynamic interaction phenomena that occur between the propeller and flat-wall boundary layer is then provided in Sec. IV. Finally, Sec. V presents how these aerodynamic phenomena can contribute to flow separation when an external pressure gradient is generated by deflecting a flap.

II. Experimental Setup

A. Wind-Tunnel Facility and Models

The experiments were performed in the closed-circuit, low-speed, low-turbulence tunnel at the Delft University of Technology. This tunnel presents a maximum freestream velocity of 120 m/s and inflow turbulence levels below 0.07% for the freestream velocities considered in this study ($V_{\infty} \leq 40$ m/s). The closed test section has a cross section of 1.8×1.25 m. A propeller was positioned in close proximity to the suction-side surface of a straight, untapered wing by means of a support sting, as shown in Fig. 1. The support sting was mounted on an external balance during propeller force measurements, as well as on a three-axes traversing system for all other measurements. Additional information regarding the geometry of the wing and propeller can be obtained from the CAD model available in Supplemental Data S1.

1. Wing Geometry and Operating Conditions

The wing profile was designed such that, close to the propeller, it is representative of a quasi-flat-plate configuration when the flap is retracted ($\delta_f = 0$ deg). The resulting profile, shown in Fig. 2b, presents a chord^{††} of $c = 1.02$ m and a thickness-to-chord ratio of

^{††}The reference chord length is taken as the length of the profile when the flap is retracted ($\delta_f = 0$ deg). Since the upper surface of the flap translates when it is deflected, the true chord varies.

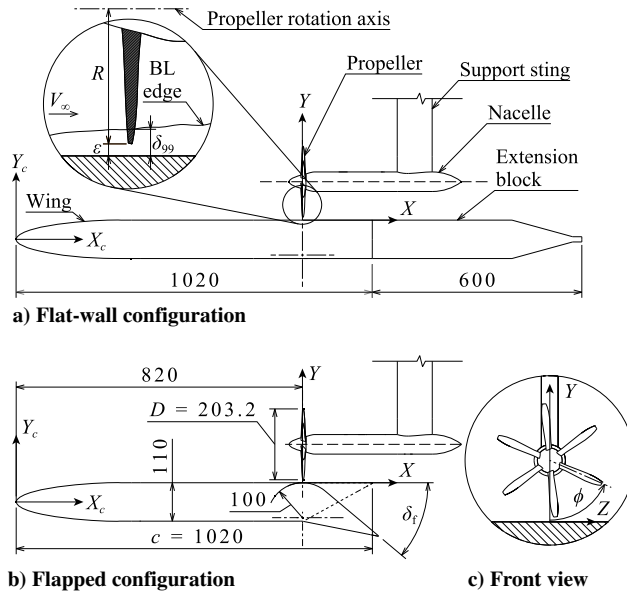


Fig. 2 Front and side views of experimental model. Dimensions expressed in millimeters. Origin of local reference frame (X , Y , Z) corresponds to $(X_c, Y_c, Z_c) = (820, 55, 0)$ mm in wing-based reference frame.

11%. The leading-edge geometry follows a modified superellipse with an aspect ratio of six up to 32% chord in order to provide a smooth transition to the flat upper and lower surfaces [39]. Both the suction and pressure sides are then extended parallel to the wing-chord line up to 80% chord, which corresponds to the axial position of the flap hinge. The flap hinge is located near the pressure side, generating a tangent circular arc with a radius of curvature equal to 10% chord on the suction side of the flap, which is approximately equal to the propeller radius. Behind the arc, the flap surface extends the remaining 20% of the chord to the trailing edge. The upper and lower surfaces of the flap can be split and aligned in axial direction in order to elongate the flat surface of the wing. In this way, by placing an additional body of the same thickness as the wing in the test section (see Fig. 2a), the pressure gradient surrounding the flap region is removed.

Measurements were carried out at $\alpha = 0$ deg and $V_\infty = 40 \pm 0.05$ m/s in order to maximize the Reynolds number ($Re_c = 2.76 \cdot 10^6$) without exceeding the maximum input level of the microphones or the maximum power of the electrical motor that drove the propeller, as well as at $V_\infty = 20 \pm 0.05$ m/s ($Re_c = 1.38 \cdot 10^6$) in order to increase the maximum thrust coefficient. Two boundary-layer configurations were tested to vary the equivalent Reynolds number of the boundary layer at the propeller location and verify whether there were any significant scaling effects that may be overlooked when using a scaled-down wind-tunnel model. The first, named “BL₁,” corresponded to the turbulent boundary layer obtained with a 3-mm-wide trip strip of distributed roughness elements with an average diameter of 530 μm (carborundum particles of grit size 36) located at 7.5% chord on both sides of the wing. The second, named “BL₂,” was a thicker turbulent boundary layer obtained by applying sandpaper of grit size 36 from 7.5 chord to 32% chord on the suction side. This was done to increase the boundary-layer thickness at the downstream propeller location without significantly changing the boundary-layer profile, as discussed in Sec. III. After analyzing multiple flap-deflection angles, an angle of $\delta_f = 20$ deg was selected to study the interaction phenomena in more detail since, for this deflection angle, the flow remained attached over the flap hinge but started to separate toward the trailing edge of the isolated wing (i.e., without propeller installed).

2. Propeller Geometry and Operating Conditions

For the majority of the measurements, the propeller was positioned above the flap hinge ($X_p/c = 0.8$), which was identified as an axial

location with a good compromise between lift gain, drag reduction, and propulsive-efficiency loss in previous work [18]. The installation was designed such that the propeller axis was located at the midspan of the wing when connected to the balance. A six-bladed steel propeller was used, with a diameter of $D = 0.2032$ m ($D/c = 0.2$) and a blade pitch of $\beta_{0.7} = 45 \pm 0.05$ deg. The propeller is a 1:2 scale model of the one used by Li et al. [40], with a modified trailing edge to ensure a minimum thickness during the manufacturing process. The propeller was operated at advance ratios between $J = 1.7$ and $J = 2.3$ at $V_\infty = 40$ m/s, as well as between $J = 1.0$ and $J = 2.0$ at $V_\infty = 20$ m/s, in order to obtain thrust coefficients and slipstream characteristics comparable to full-scale aircraft. For the baseline measurement conditions ($V_\infty = 20$ m/s, $J \approx 1.1$), this corresponds to approximately 5300 rpm, a tip Mach number of $M_{\text{tip}} = 0.18$, and a blade Reynolds number of $Re_{0.7} = 4.2 \cdot 10^4$. Previous numerical and experimental analyses of the propeller [41] showed that the radial loading distribution varies slightly with Mach number and that the integral thrust increases with Reynolds number, but without any qualitative changes in the behavior of the propeller. Therefore, although the quantitative results may vary, the conceptual interpretation of the phenomena observed in the experiment was considered applicable to a full-scale distributed-propeller configuration in takeoff or landing conditions. The rotational speed of the propeller was controlled with an accuracy of ± 0.1 Hz that, together with the velocity uncertainty, corresponds to fluctuations in the advance ratio below $\pm 0.5\%$. Furthermore, the clearance between the propeller blade tips and the wing surface ϵ was varied in order to analyze the impact of tip clearance on the interaction effects (see Sec. III). Finally, a subset of measurements was taken with the propeller at $X_p/c = 0.75$ in order to determine the influence of the propeller’s axial position on flow separation.

B. Measurement Techniques

The following subsections provide an overview of the measurement techniques used during the experiment. The measured velocities and pressures were corrected for wind-tunnel blockage caused by the wing, following the image method described in Ref. [42]. Lift interference corrections were not applied since only low lift coefficients were attained ($c_l \approx 0.1$). Propeller slipstream and support-sting blockage corrections were neglected since their combined effect on the velocity was estimated to be below 0.9%.

1. External Balance

The propeller was installed on an external six-component balance to measure propeller thrust. The balance presented an uncertainty of ± 0.02 N in the range of forces measured in the experiment, which corresponds to approximately 0.4% at high thrust ($C_T = 0.35$) and 1.2% at medium thrust ($C_T = 0.2$). Data were acquired at 10 Hz, and each measurement point was averaged over 30 s. Several measurements were repeated twice to verify the reproducibility of results. To obtain the net forces generated by the propeller blades and spinner, all measurements were carried out with both the propeller on (indicated with the subscript “on”) and with the propeller removed and replaced by a dummy spinner (indicated with the subscript “off”). The net thrust T is then defined as $T = T_{\text{on}} - T_{\text{off}}$. It should be noted that the thrust force therefore includes the change in drag on the nacelle and support sting due to the propeller slipstream.

The uncertainty of the thrust measurements was calculated by taking into account uncertainties in the blade pitch angle, propeller alignment, and balance readings, as well as the data spread of repeated measurements due to, for example, variations in operating conditions. For this, the sensitivity of propeller thrust to blade pitch angle ($\partial T / \partial \beta$) and angle of attack ($\partial T / \partial \alpha_p$) were obtained from experimental and numerical data of the isolated propeller [41]. The resulting thrust-coefficient uncertainty was below 1% at high thrust ($C_T = 0.35$) and below 3% at medium thrust ($C_T = 0.2$).

2. Total-Pressure Probe

A pressure probe was traversed in the Y direction at $X_c/c = 0.8$ to determine the boundary-layer profiles of the isolated wing at the axial

position of the propeller disk. The measurement sweep started at 0.5 mm ($0.005R$) clearance from the wing surface, and it was traversed up to 240.5 mm ($2.37R$) clearance. The pressure was measured at 57 locations for each of the three spanwise positions sampled ($Z/R = 0, -0.9$, and $+0.9$), with a higher resolution in the vicinity of the wing surface. Pressure data were acquired at 10 Hz and averaged over 30 s for each point using a DTC-Initium pressure scanner. The measurement uncertainty of the total-pressure sensors (± 4 Pa) and the spread in data due to spanwise variations in the boundary-layer profile led to a total-pressure-coefficient uncertainty below 2% of the freestream value. The boundary-layer thickness δ_{99} was determined as the distance from the surface where the total pressure reached 0.99^2 times the total pressure of the freestream; that is, where $C_{p,t} = 0.98$.

3. Wing Surface-Pressure Taps

The wing was instrumented with 81 static-pressure taps in order to evaluate the time-averaged impact of the propeller on the wing pressure distribution. These taps were distributed with a higher density near the leading edge and near the flap hinge. The holes were located along a zigzag pattern at $Z = \pm 15$ mm, i.e., 15 mm above or below the midspan location of the wing. Due to the geometrical constraints surrounding the flap mechanism, no zigzag pattern was followed in this region, as is visible in Fig. 3. Data were acquired at 10 Hz and averaged over a 30 s acquisition time per measurement point. A subset of measurements was repeated at the start and the end of the experiment to verify the reproducibility of results. The spread in the data of the repeated measurements, along with the uncertainty of the static-pressure sensors of the pressure scanner (± 1 Pa), contribute to a pressure-coefficient uncertainty of approximately ± 0.025 .

Two types of static-pressure measurements were taken. In the first, the propeller was installed on an external traversing system and moved in the Z direction, mapping the pressure response on the wing surface below the propeller. For these measurements, the propeller was traversed 150 mm in each direction ($Z/R = \pm 1.5$), sampling at 51 spanwise locations in total. In the second type of measurement, the propeller (connected to the balance) was positioned at the midspan of the wing, and the pressure distribution was recorded along the line of pressure taps. In this case, the resulting pressure distribution did not correspond exactly to the midsection of the wing, due to the zigzag pattern. The difference was quantified by analyzing the spanwise pressure distribution obtained during the Z sweeps, and included as uncertainty in the results.

4. Wing Surface Microphones

The wing was instrumented with 19 Sonion 8044 microphones in order to map the unsteady pressure response on the wing surface below the propeller slipstream. Twelve microphones were installed on the flap (at $Z = 35$ mm), and seven were installed on the main wing immediately upstream of the flap (at $Z = -35$ mm), as indicated in Fig. 3. The microphones measured in a frequency range

of 20 Hz–15 kHz, with a maximum input level of 123.5 dB (relative to $20 \cdot 10^{-6}$ Pa) at 1 kHz and an equivalent noise level of 35 dBA. A frequency-dependent calibration was carried out using a LinearX M53 reference microphone, which was in turn calibrated by means of a GRAS 42AA pistonphone.

Microphone data were acquired synchronously with the propeller encoder's once-per-revolution trigger signal using an array of National Instruments 9234 data acquisition (DAQ) modules. The microphone data were recorded in tandem with the wing pressure data during the Z sweeps of the propeller. At each point, the signals were measured at a sampling frequency of 51.2 kHz during 30 s, which corresponds to approximately 1500 to 3500 propeller revolutions (i.e., 9000 to 21,000 blade passages), depending on the rotational speed of the propeller. Although no quantitative uncertainty analysis was carried out, a comparison of repeated measurements showed that the amplitude of the tonal components differed by less than 1 dB. Furthermore, the levels recorded during the measurements were verified to be at least 25 dB (typically 45 dB) above the background noise levels recorded with the wind tunnel off.

5. Particle Image Velocimetry

A stereoscopic particle image velocimetry (PIV) setup was used to analyze the velocity field in the propeller slipstream and wing boundary-layer. Two fields of view were considered. The main, large field of view (FOV) was set up downstream of the flap hinge (i.e., downstream of the propeller disk location), as shown in Fig. 3. A second high-resolution FOV focused on the region surrounding the blade tips. A SAFEX Twin Fog DP generator with SAFEX-Inside Nebelfluid was used for flow seeding. The mixture of diethylene-glycol and water generates tracer particles with an average diameter and relaxation time below 1 μm and 1 μs , respectively. A 200 mJ Quantel Evergreen laser was used for illumination and positioned outside the test section on the pressure side of the wing. The light was directed through the wing with a dedicated slit in the wing and flap skin (see Fig. 1b), generating a laser sheet of 2 mm thickness. Both slits were covered with a transparent plastic sheet of 0.2 mm thickness to prevent the throughflow of air. Two 16-bit LaVision Imager sCMOS cameras were used for image acquisition, which feature a 2560×2160 pixel sensor with a pixel size of 6.5 μm , and were employed with Nikkor 105 mm $f/8$ and Nikkor 200 mm $f/8$ lenses for the large and small FOVs, respectively. The images were recorded at 15 Hz and processed using LaVision Davis 8.4 software. For installed propeller measurements, 600 uncorrelated images were acquired, in addition to 300 phase-locked images at selected phase angles and 300 images with the propeller blades removed (i.e., wing and nacelle only). The main characteristics of the PIV setup are gathered in Table 1.

For two measurement cases, phase-locked PIV data were acquired at different Z locations relative to the propeller by positioning the propeller at different spanwise locations along the wing. The resulting velocity fields were combined to obtain a volumetric dataset that provides three-dimensional information of the flowfield. The distance between adjacent measurement planes varied from 2.5 to 10 mm, which constituted a relatively low spanwise resolution. Thus, during the post-processing, the velocity fields were interpolated on additional planes between each pair of measurement planes to improve the visualization of the blade wakes and tip vortices.

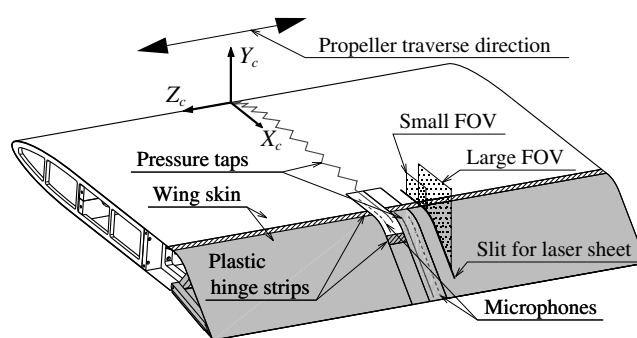


Fig. 3 Axonometric view of suction side of wing model, indicating location of pressure taps, microphones, and PIV plane. Elements that constitute flap shaded in gray.

Table 1 Main parameters of the PIV setup

FOV	Large	Small
Focal length, mm	105	200
Field of view, mm ²	100×150	50×65
Pixel shift, pixel (at V_∞)	9.5	8.2
Imaging resolution, pixel/mm	19	41
Window size, pixel ²	24	24
Overlap factor, %	50	50
Vector spacing, mm	0.6	0.3
Velocity uncertainty, %	2.5	2.75

For this, it was assumed that the flow structures present in a measurement plane Z_1 were also present in the adjacent measurement plane Z_2 , but with an in-plane displacement ($\Delta X, \Delta Y$). This displacement vector was estimated by performing two-dimensional cross correlations for each point (X, Y) on the two planes. The flowfield quantities were then computed on a series of intermediate query planes Z_q by linearly interpolating between Z_1 and Z_2 along the interpolation direction obtained from the cross correlation. This ensured the continuity of the isosurfaces representing the vortex filaments and blade wakes.

III. Isolated-Wing Characteristics

This section describes the aerodynamic characteristics of the isolated wing, to establish the conditions under which the interaction effects are studied in subsequent sections. Figure 4 shows the pressure-coefficient distributions obtained on the wing surface, with the propeller and support sting removed. When the flap is deflected by $\delta_f = 20$ deg, an appreciable pressure peak is generated over the flap, as shown in Fig. 4. The pressure gradient on the suction side tends toward zero near $X_c/c = 1$, indicating that the flow has separated at the trailing edge. A suction peak is also generated on the pressure side, since the surface is convex near the flap hinge. Together, this leads to a low sectional lift coefficient of $c_l = 0.1$. Moreover, a small pressure peak is generated around $X_c/c = 0.08$ by the trip strip, whereas additional suction is generated around $X_c/c = 0.22$ due to a flaw in the curvature of the wing skin. However, these peaks occur relatively far (approximately six radii) upstream of the propeller location, and therefore have a negligible impact on the interaction phenomena.

In the flat-wall configuration, the difference between the pressure and suction sides of the wing is negligible; and the pressure gradient is small for $X_c/c > 0.4$. However, several imperfections are visible. First, small pressure peaks are generated around $X_c/c = 0.8$ due to steps in the surface geometry at the overlap from the main element to the flap. Second, toward the trailing edge, the difference between the pressure side and suction side increases, indicating that the flap surfaces—which were aligned with the downstream extension block (see Fig. 2)—were not perfectly parallel. These imperfections may affect the development of the boundary layer, and therefore it is necessary to determine the boundary-layer profiles inherent to this experimental setup. Nevertheless, the average pressure-coefficient increase across the propeller disk (which can be calculated by dividing the propeller thrust by the disk area) ranges from approximately 0.2 at medium thrust to 0.6 at high thrust. Thus, the local pressure variations due to surface imperfections are small, and the interaction phenomena are dominated by the effect of the propeller.

The boundary-layer profiles are presented for different configurations and operating conditions in Fig. 5. The effect of an increase in equivalent surface roughness can be observed by comparing the two flat-wall profiles at $V_\infty = 40$ m/s: when the boundary layer is tripped (BL₁), the boundary-layer thickness is $\delta_{99}/R = 0.14$; whereas with an increase in surface roughness (BL₂), the thickness increases to $\delta_{99}/R = 0.20$. This 43% increase in boundary-layer thickness corresponds to an increase in the equivalent turbulent flat-plate Reynolds number from $Re_{FP} = 1.8 \cdot 10^6$ to $Re_{FP} = 2.8 \cdot 10^6$ ^{††}. The measurements at $V_\infty = 20$ m/s, on the other hand, both correspond to BL₁. Under those conditions, the flat-wall boundary layer is thicker than the one obtained with the flap deflected due to the increased velocity over the wing in the flap-deflected case. When comparing the flat-wall boundary layers (BL₁) at 20 and 40 m/s, it appears that the former is thicker, as expected, but also presents a fuller profile than the latter. This suggests that the surface geometry was altered between the two measurements, most likely due to changes in the plastic hinge strips (see Fig. 3), which are situated near the measurement location.

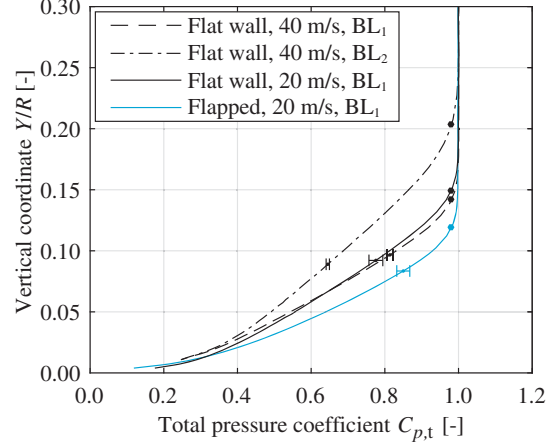


Fig. 5 Boundary-layer profiles on the wing surface at $X_c/c = 0.8$, with the propeller and support sting removed. Round markers indicate the vertical coordinate corresponding to δ_{99} .

Table 2 Summary of the measured boundary-layer configurations and propeller tip-clearance values

Configuration	δ_{99}/R	ϵ/R
Flat wall, BL ₁ (40 m/s)	0.14	0.07 ($\frac{1}{2}BL_1$)
		0.14 (1 BL_1)
		0.28 (2 BL_1)
Flat wall, BL ₂ (40 m/s)	0.20	0.10 ($\frac{1}{2}BL_2$)
		0.20 (1 BL_2)
		0.40 (2 BL_2)
Flat wall, BL ₁ (20 m/s)	0.15	0.037 ($\frac{1}{4}BL_1$)
		0.07 ($\frac{1}{2}BL_1$)
		0.15 (1 BL_1)
$\delta_f = 20$ deg, BL ₁ (20 m/s)	0.12	0.037 ($\frac{1}{4}BL_1$)
		0.07 ($\frac{1}{2}BL_1$)
		0.15 (1 BL_1)
		0.44 (3 BL_1)

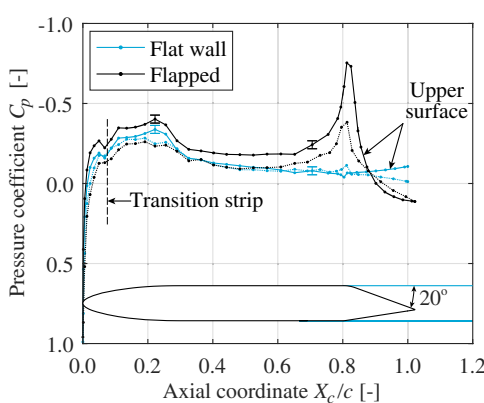


Fig. 4 Isolated-wing pressure distributions in the flat-wall and flapped configurations ($V_\infty = 20$ m/s, BL₁).

The values of δ_{99} are summarized in Table 2. The propeller tip-clearances analyzed in Secs. IV and V were selected as fractions or integer multiples of these values. Note that, when the flap is deflected, the propeller tip clearance is still selected as a fraction or multiple of the flat-wall boundary-layer thickness. In this way, the same absolute separation between the blade tips and the wing surface (ϵ/R) was kept, and thus the time-averaged pressure effect of the propeller on the wing is maintained.

^{††}The equivalent turbulent flat-plate Reynolds number is defined as $Re_{FP} = (\rho_\infty V_\infty X_{FP})/\mu$, where X_{FP} is the distance to the virtual origin of the equivalent flat plate, which is computed using $\delta_{99} = 0.37 X_{FP} (\rho_\infty V_\infty X_{FP}/\mu)^{-0.5}$ [43].

IV. Aerodynamic Interaction with a Flat-Wall Boundary Layer

This section describes how the propeller interacts with the boundary layer developing over a wing without axial pressure gradients. In this configuration, the boundary-layer thickness and propeller tip clearance were found to have a negligible effect on propeller thrust (see Fig. A1 of the Appendix). The interaction effects are decomposed into a steady component (Sec. IV.A) and an unsteady component (Sec. IV.B). In both cases, the phenomena are presented for high thrust and low tip clearance ($BL_1, V_\infty = 20 \text{ m/s}$, $C_T = 0.35$, and $\epsilon/R = 0.037$), unless explicitly mentioned otherwise.

A. Time-Averaged Flow Phenomena

The velocity distributions between the nacelle and the wing surface in the flat-wall configuration are shown in Fig. 6. In propeller-off conditions, the axial velocity in this region is slightly higher than the freestream velocity due to the presence of the nacelle and wing (Fig. 6a). When the propeller is installed and operated at a high thrust setting (Fig. 6b), the axial velocity in the slipstream is increased, especially near the radial location of highest loading ($r/R \approx 0.7$). Immediately downstream of the propeller disk, near the surface, a region of low axial velocity is observed. The low-velocity region is originated directly beneath the propeller disk due to slipstream contraction close to the wall, and it persists until the flow has convected approximately half a propeller radius downstream. Beyond that point, the slipstream approaches the wall and the velocity near the surface increases. This effect is further evidenced in Figs. 6c and 6d.

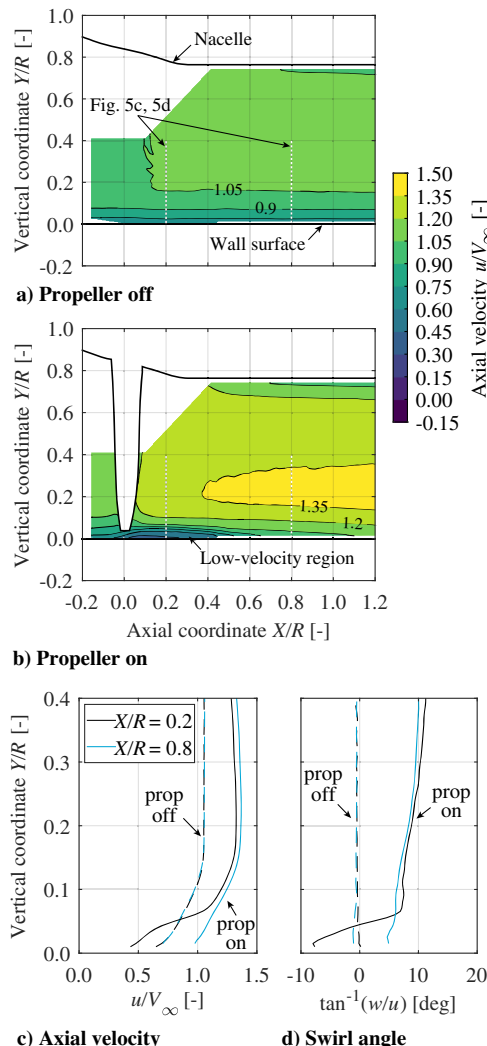


Fig. 6 Time-averaged velocity distribution between the nacelle and the flat wall ($Z/R = 0$). (Prop denotes propeller.)

At $X/R = 0.2$, the flow velocity near the wall is lower than in the propeller-off case, although no reverse flow is observed. The swirl angle, however, is opposed to the swirl inside the slipstream. At $X/R = 0.8$, on the other hand, the velocity is higher near the wall. Moreover, a significant swirl angle remains in the vicinity of the wall. This indicates that the edge of the slipstream has approached the wall since, in a time-averaged sense, swirl is only generated inside the propeller slipstream. The cause of this vertical displacement is described in Sec. IV.B.3.

The corresponding surface-pressure field induced by the propeller is shown in Fig. 7. In this figure, the static pressure measured in the propeller-off case has been subtracted (i.e., $\Delta C_p = C_{p,\text{on}} - C_{p,\text{off}}$) to remove the effect of the nacelle. The static-pressure jump created across the propeller disk leads to a decrease in pressure on the wall upstream of the propeller, as well as an increase in pressure downstream of it. Although at low thrust settings and large tip clearances the effect on the wing surface is weak, at higher thrust settings and smaller clearances the effect on the wing surface is strong, as expected from earlier studies [18,32,44]. The pressure peak created downstream of the propeller, however, is not. This is due to the tangential momentum imparted to the flow by the propeller, which leads to a spanwise velocity component near the wall, as reflected in Fig. 6d.

Between the two pressure peaks observed in Fig. 7, a strong adverse pressure gradient is generated. The magnitude of this adverse pressure gradient is directly proportional to the propeller's thrust, since it is governed by the pressure jump across the disk. This is shown in Fig. 8, where the parameter C_T/J^2 is used on the x axis to exclude the effect of rotational speed from the nondimensionalization. It should be noted that these measurements were performed at 40 m/s, and therefore do not reach the high thrust coefficients of Figs. 6b or 7b ($C_T < 0.25$). The slopes of the curves increase with decreasing tip clearance while showing no significant dependency on the boundary-layer thickness, although additional measurements at constant tip clearance and different boundary-layer thicknesses would be required to quantify this. This suggests that the time-averaged adverse pressure gradient generated beneath the propeller can be captured by lower-order methods such as actuator-disk models.

B. Unsteady Flow Phenomena

Additional insight into the interaction mechanisms can be gained by analyzing the unsteady flow structures in the propeller slipstream.

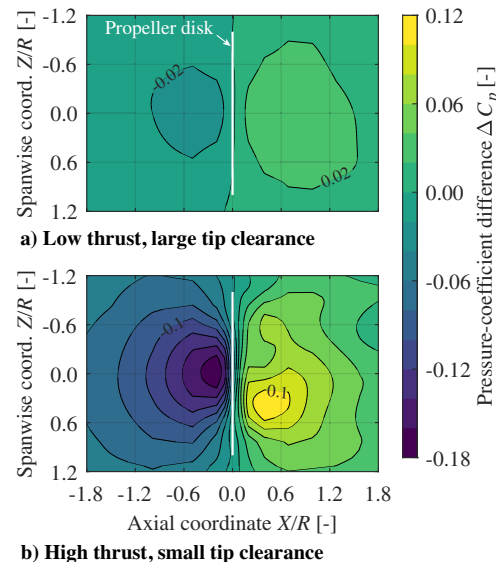


Fig. 7 Pressure distribution induced by the propeller on the wing surface in flat-wall configuration. Measurements performed at a) $V_\infty = 40 \text{ m/s}$, $C_T = 0.2$, and $\epsilon/R = 0.14$; and b) $V_\infty = 20 \text{ m/s}$, $C_T = 0.35$, and $\epsilon/R = 0.037$. (Coord. denotes coordinate.)

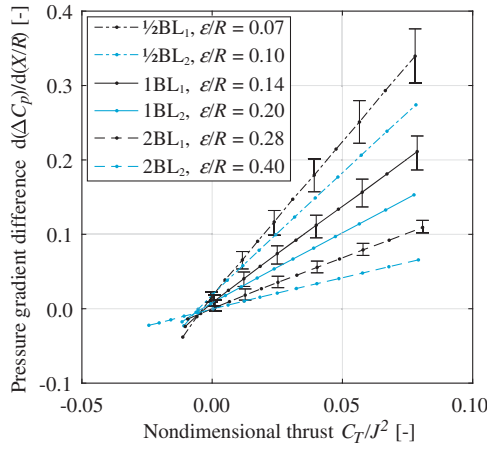


Fig. 8 Nondimensional pressure gradient generated by the propeller on the wing surface below the propeller disk in the flat-wall configuration ($V_\infty = 40$ m/s).

To this end, the aerodynamic interaction between the tip vortices and the wing boundary layer is first assessed in Sec. IV.B.1 by analyzing the local velocity fields. The pressure fluctuations generated on the wing surface by these flow structures are then described in Sec. IV.B.2. Finally, the velocity and pressure distributions are combined to provide a volumetric description of the evolution of the tip vortices in Sec. IV.B.3.

1. Vortex/Boundary-Layer Interaction

Figure 9 presents the phase-averaged spanwise vorticity distribution in the $Z/R = 0$ plane for three different phase angles. The nondimensional vorticity is defined as $\tilde{\omega}_z^* = \tilde{\omega}_z D/u_{\text{eff}}$, where u_{eff} is the theoretical velocity at the propeller disk, as obtained from actuator-disk theory for a given thrust coefficient [45]. For this measurement, the thrust coefficient corresponds to an effective velocity of $u_{\text{eff}} = 1.13V_\infty$. The propeller tip vortices appear in Fig. 9 as regions of highly concentrated (negative) spanwise vorticity. The vorticity contained in the blade wakes, on the other hand, switches sign in accordance with the spanwise loading gradient along the propeller blade. The negative vorticity in the boundary layer is also visible near the wall. When comparing the three time instances, it

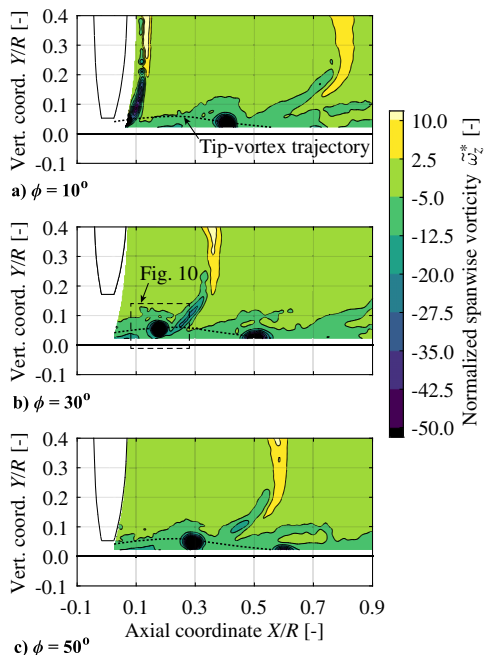


Fig. 9 Phase-averaged spanwise vorticity distribution in the propeller slipstream. (Vert. denotes vertical.)

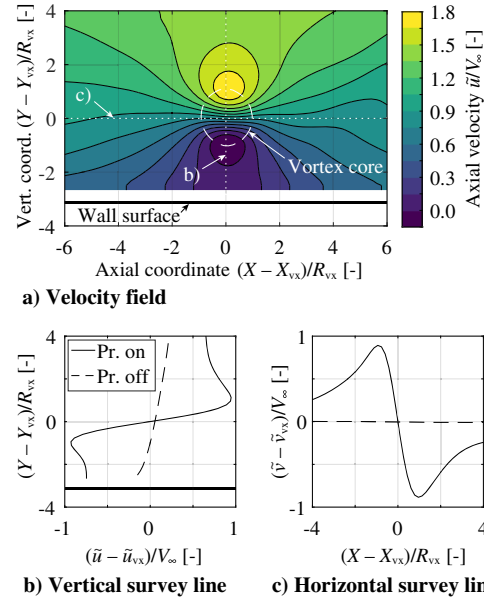


Fig. 10 Phase-averaged velocity distribution relative to the propeller tip vortex ($\phi = 30$ deg, $R_{vx}/R = 0.017$).

becomes evident that the tip vortices initially move away from the wall and subsequently, beyond $X/R \approx 0.25$, start to approach the wall again. The trajectory followed by each tip vortex approximately delimits the low-speed region observed in Fig. 6.

The velocity field surrounding the vortex indicated in Fig. 9b is analyzed in more detail in Fig. 10 to verify whether the viscous shear between the boundary layer and the vortices is responsible for their downward displacement. The axes of Fig. 10 are expressed relative to the center of the vortex core, for which the point of maximum out-of-plane vorticity $\tilde{\omega}_z$ is selected. Figure 10a also indicates the boundaries of the vortex core, defined by the radial coordinate where the tangential velocity with respect to the center of the vortex is maximum. The average distance to the vortex center is then taken as the vortex radius R_{vx} . It is worth noting that this “phase-averaged vortex core” is larger than the vortex core that would be identified in an instantaneous velocity field. This occurs because, for the same phase angle, the tip vortices are located at slightly different positions from one blade passage to another due to the random interaction with the turbulent eddies in the boundary layer. This random behavior was confirmed by comparing the instantaneous velocity fields obtained from PIV (not shown here). The flowfield of Fig. 10a shows that, on average, a region of negative velocity is induced beneath the vortex, although at the wall no flow reversal is observed.

More insight can be gained by extracting two survey lines, shown in Figs. 10b and 10c. These plots present two velocity profiles, expressed relative to the velocity at which the vortex core is convected ($\tilde{u}_{vx}, \tilde{v}_{vx}$). Figure 10b shows that the axial-velocity profiles above and below the vortex center are roughly antisymmetric, but it also shows that the top half tends asymptotically to a higher absolute axial velocity than the lower half. This is due to the superimposed effect of the boundary-layer profile and image vortex. The vertical velocity on the horizontal survey line (Fig. 10c), on the other hand, tends toward zero on either side of the vortex core, despite the presence of the viscous boundary layer. The shear stresses on either side of the vortex therefore counteract each other, which suggests that no appreciable net vertical force is exerted on the vortex core. These findings are in line with the predictions of Doligalski and Walker [31] and Chuang and Conlisk [29], who studied the response of a convecting rectilinear vortex near a wall and defined the ratio between the convection speed of the vortex core and the uniform inflow velocity α as

$\ddagger\ddagger$ Note that the local “effective” uniform inflow velocity at the vortex location is unknown since it is affected by the presence of both the boundary layer and the propeller slipstream ($u_\infty \neq V_\infty$).

$$\alpha = \frac{u_{vx}}{u_\infty} = 1 + \frac{u_{ind}}{u_\infty} \quad (1)$$

where u_{ind} is the velocity induced by the image vortex, such that $u_{vx} = u_\infty + u_{ind}$. The velocity induced by the image vortex accounts for both the vortex strength Γ_{vx} and distance to the wall ε_{vx} since $u_{ind} = \Gamma_{vx}/(4\pi\varepsilon_{vx})$. The circulation of the vortex core can be obtained by integrating the vorticity inside the core ($\Gamma_{vx,core} = -0.19 \text{ m}^2/\text{s}$). By assuming that this is approximately equal to the total circulation of the vortex ($\Gamma_{vx} \approx \Gamma_{vx,core}$) and extracting the convective velocity and vortex position from Fig. 10a, a velocity ratio of $\alpha = 0.85$ is obtained from Eq. (1). For this value, the interaction with the boundary layer, has a negligible effect on the vertical position of the vortex [29]. Moreover, in the inviscid limit, no flow reversal should occur near the wall for $\alpha > 0.75$ [31], which is consistent with the velocity field of Fig. 10a. Although the exact limit differs for viscous flow [31], the velocity ratio obtained in this experiment appears to be beyond this limit. This confirms that the vertical displacement of the tip vortices is not caused by viscous interaction with the boundary layer but by additional effects that are not captured in this simplified analysis, such as pressure gradients or three-dimensional effects.

2. Propeller-Induced Surface-Pressure Fluctuations

The vortex cores are not visible downstream of $X/R \approx 0.6$ in the FOV of Fig. 9. To further investigate this effect, the rms of the surface-pressure fluctuations is shown in Fig. 11. Directly beneath the propeller, at the locations indicated with crosses, the maximum excitation amplitude of the microphones was exceeded. Therefore, the values in this region are conservative, and no quantitative comparisons should be made. Nevertheless, several important qualitative observations can be made based on the unsteady pressure distributions. With these observations, it is possible to distinguish three different regions of pressure fluctuations, as indicated in the bottom part of Fig. 11.

First, the rms of the surface-pressure fluctuations is larger than the time-averaged surface-pressure difference induced by the propeller (see Fig. 7). This indicates that the discrete blade passages generate large differences between the maximum and minimum surface pressures, which could be reduced by producing the same thrust with a higher number of blades. Second, two distinct regions of pressure fluctuations can be observed in Fig. 11: fluctuations induced by the

propeller blades (bound vorticity), and fluctuations induced by the tip vortices (trailing vorticity). Upstream of the propeller, the surface-pressure fluctuations are dominated by the static-pressure fields surrounding each propeller blade, which are approximately constant in a rotating reference frame but lead to periodic perturbations in an inertial reference frame. “Far” downstream of the propeller, the surface-pressure fluctuations are dominated by the flow structures convected in the slipstream. Between these two regions, the two contributions are superimposed. Moreover, although Fig. 9 shows that the blades’ trailing vorticity rapidly concentrates in the tip vortices, the surface-pressure fluctuations produced by the bound vorticity are appreciably larger than the ones produced by the trailing vorticity. This occurs for two reasons. On one hand, the bound vorticity perceives a much higher inflow velocity since the blade-tip velocity ratio V_{tip}/V_∞ is approximately 2.6, whereas the vortex convection velocity is comparable to the local flow velocity ($\tilde{u}_{vx}/V_\infty \approx 0.8$). Furthermore, the radial velocity component at the propeller disk is small, and thus the bound vorticity is perpendicular to the local velocity. The tip vortices, on the other hand, form an oblique angle with the local flow velocity (see Sec. IV.B.3), further reducing their effective inflow velocity. Consequently, following the Kutta–Joukowski theorem, the bound vorticity creates larger pressure differences than the trailing vorticity, for the same circulation.

Figure 11 also shows that downstream of the propeller, the streak of high-amplitude fluctuations splits in two. The pressure spectra recorded at locations B and C, shown in Fig. 12, indicate that the region of low rms between the two streaks only presents a weak tonal component at the blade passage frequency (BPF; in hertz). However, in the streak of increased rms, as well as at point A, the pressure spectrum is dominated by high-amplitude peaks at the blade passage frequency and multiple harmonics. Therefore, whereas at locations A and B sharp wave forms are generated by the passage of the propeller blades and tip vortices, respectively, at point C, these excitations are barely perceived.

The mechanism that causes the high-rms region to divide in two can be understood by analyzing the interaction of the tip vortices with the solid surface. However, the axial measurement resolution is relatively low, being of the same order of magnitude as the wavelength of the dominant excitation in this region. Hence, the axial plotting resolution is artificially increased tenfold by reconstructing the pressure history between subsequent axial measurement locations, similar to the work performed in Ref. [46]. Given that not all measurements were acquired synchronously, only the phase-averaged wave forms are reconstructed. Figure 12 shows that the tonal excitations are dominant, and thus only a negligible amount of information is lost by removing the broadband component of the fluctuations. Moreover, since these pressure perturbations are hydrodynamic in nature, they propagate according to the local flow and boundary conditions, and not as acoustic waves. Upstream of the propeller ($X/R < 0$), the tonal pressure fluctuations displace in the positive Z direction, following the local movement of the blades.

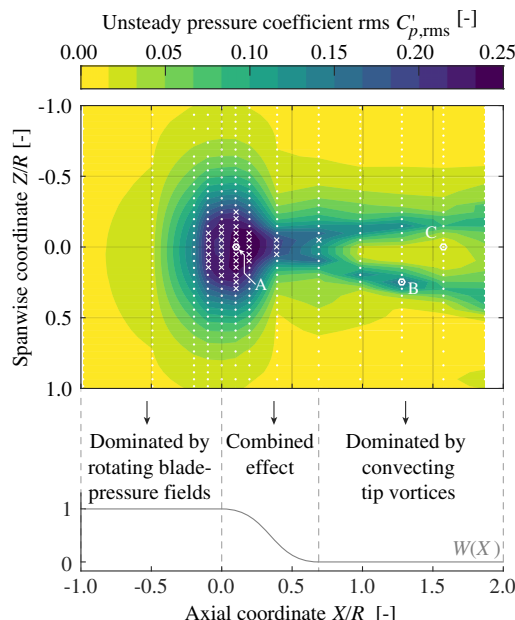


Fig. 11 Unsteady pressure-coefficient rms contours on the wall surface. Dots indicate measurement locations, whereas crosses indicate locations where the maximum input level of the microphone was exceeded.

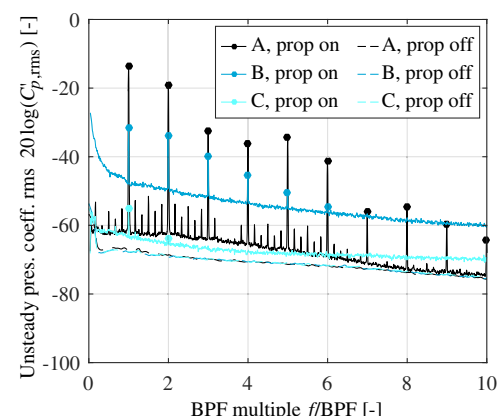


Fig. 12 Surface-pressure spectra recorded at the locations indicated in Fig. 11. Note that the maximum excitation amplitude of the microphone was exceeded at location A in the propeller-on case. $\text{BPF} = 482 \text{ Hz}$.

Therefore, in this region, the pressure at a generic X coordinate is computed by linearly interpolating between the upstream and downstream measurement locations, without considering any time delays. Far downstream of the propeller ($X/R > 0.7$), the pressure fluctuations displace mainly in axial direction, convected at the local flow velocity. For each interpolation location in this region, the convective velocity is estimated by performing a cross correlation between the tonal wave forms of the upstream and downstream measurement locations. With this convective velocity, the temporal evolution of pressure at a determined X location can be reconstructed through interpolation, as described in Ref. [46]. Finally, in the overlap region ($0 < X/R < 0.7$), a sigmoid weighting function $W(X)$ is applied to provide a smooth transition between the two excitation sources, as shown in Fig. 11.

The pressure-reconstruction process presents some uncertainty for several reasons, such as outliers in the estimated convective-velocity distribution, and the arbitrary choice of a sigmoid weighting function. Therefore, for validation, the instantaneous pressure distributions are compared to the phase-locked vorticity field obtained from the PIV measurements in Fig. 13. This figure shows the spanwise vorticity distribution in the $Z/R = 0$ plane together with the phase-averaged surface-pressure distribution for a phase angle of $\phi = 35$ deg. The pressure distribution contains both the time-averaged component acquired with the pressure taps and the unsteady component acquired with the microphones. Beneath the tip vortices, whose location can be clearly identified in the vorticity field, regions of low pressure are observed. Peaks of low pressure are also induced ahead of the propeller blades, which are responsible for the low-pressure area shown upstream of the propeller disk in Fig. 7. A time-resolved animation, available in Supplemental Data S2, shows that the location of the suction peaks on the surface is consistent with the position of the propeller blades and tip vortices, for all phase angles. This indicates that the pressure reconstruction is, at least qualitatively, correct. Moreover, a comparison of different phase angles shows how the suction peaks created ahead of the propeller are strongest when the blade tip is closest to the wall ($\phi \approx 0$ deg). The strength of the pressure fluctuations induced by the tip vortices decreases as they are convected downstream, especially in the $Z/R = 0$ plane.

3. Tip-Vortex Deformation

To determine how the slipstream structures evolve outside the $Z/R = 0$ plane, Fig. 14 presents a close-up view of the blade-tip region for a phase angle of $\phi = 5$ deg. The vortex trailing behind the blade tip is clearly identifiable in the vorticity field. The figure confirms that the low-pressure region generated beneath the tip vortices is also captured outside of the $Z/R = 0$ plane. For this blade angle, a strong suction peak is generated on the wall ahead of the

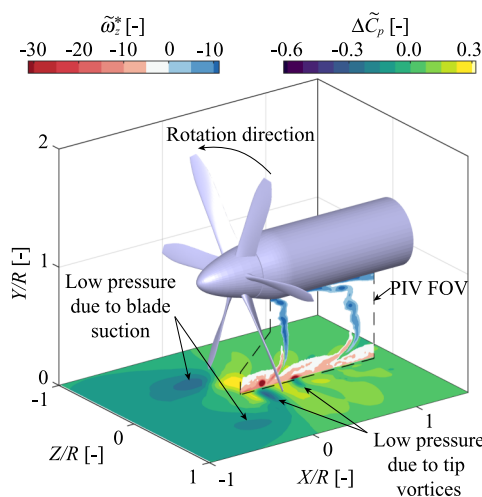


Fig. 13 Comparison of phase-averaged surface-pressure and slipstream-vorticity distributions for $\phi = 35$ deg. Vorticity contours only shown for $|\tilde{\omega}_z^*| > 2$.

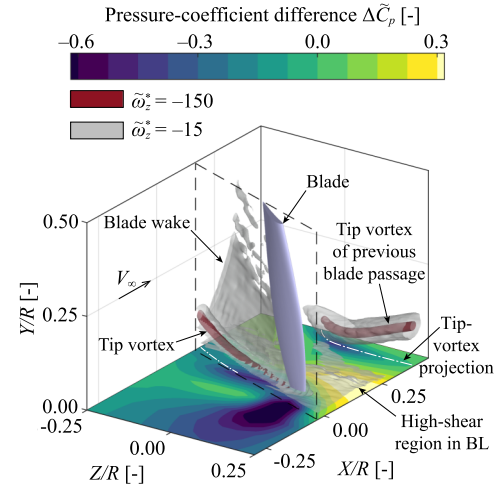


Fig. 14 Phase-averaged surface-pressure distribution and vorticity isosurfaces in the vicinity of the propeller blade tip for $\phi = 5$ deg. Vorticity isosurfaces only shown downstream of the plane indicated by dashed black lines.

suction side of the blade. Downstream of the propeller blade, a $\tilde{\omega}_z^* = -15$ isosurface is present near the wall, due to the strong vertical gradient of axial velocity in the boundary layer. At this location, the pressure at the wall has increased due to the increased static pressure behind the blade and the associated slipstream contraction.

In Fig. 14, the projection of the downstream tip vortex onto the wall is curved and suggests that the vortex filament has deformed. This can be confirmed by analyzing the unsteady pressure distribution on the wall for a determined phase angle, as shown in Fig. 15. This figure includes the projection of the tip vortices, which are drawn based on the $\Delta\tilde{C}_p$ distribution and on the data presented in Figs. 9 and 11. In an undisturbed slipstream, the tip vortices follow a helical path, and thus these projections would locally appear as oblique lines positioned at an angle equal to the pitch of the helix, with a weak inflection point at $Z/R = 0$. However, due to the presence of the wall, the vortex segments closest to the wall are convected at a lower axial velocity. Consequently, the segments below the propeller axis ($Z/R = 0$) start to lag, and the vortices deform. This is clearly visible for the second vortex ("Vx. 2") in Fig. 15. Due to the downward displacement of the slipstream, the central part of the vortex filament eventually

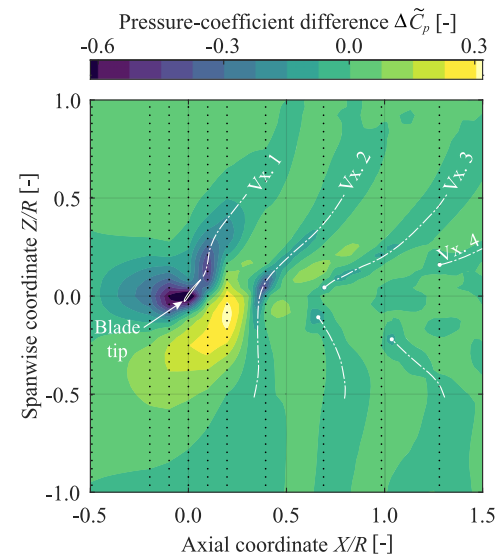


Fig. 15 Phase-averaged surface-pressure-coefficient distribution beneath the propeller slipstream for $\phi = 0$ deg. Data based on microphone measurements; i.e., mean pressure is not included.

approaches the wall and splits in two, as can be seen for the third and fourth vortices.

Finally, a schematic representation of the phenomena observed in Figs. 7–15 is drawn in Fig. 16 to explain the downward displacement of the slipstream. When the tip vortex is originally formed behind the blade, it follows a helical path (point A). Due to the strong pressure jump across the propeller disk, the slipstream contracts and the tip vortex moves away from the wall (point B). However, the pressure increase behind the disk also leads to a spanwise pressure gradient on the wall. The spanwise gradient accelerates the flow away from the $Z/R = 0$ plane. This in turn creates a mass deficit near the wall in the $Z/R = 0$ plane, which leads to fluid entrainment from the slipstream above. Since the slipstream contraction rate rapidly diminishes downstream of the disk (as known from actuator-disk theory; see, e.g., Ref. [45]), beyond a determined point B, the effect of the spanwise gradient becomes dominant and causes the slipstream to move downward. Simultaneously, the vortex filament is deformed due to the lower convective velocity near the wall. For the thrust coefficient and advance ratios studied in this experiment, an undisturbed helical vortex would constitute a stable structure, which only self-induces axial velocities [47]. However, due to the local deformation of the tip vortex, this equilibrium is lost, and the vortex filament self-induces a velocity in the negative Y direction in the $Z/R = 0$ plane (point C). This further contributes to the downward displacement of the slipstream. Eventually, the tip vortex comes in very close proximity to the wall, where the axial velocity tends to zero due to the no-slip condition. The associated deformation and dissipation cause the central segment of the filament to split in two (point D). Since, at the wall, no normal velocities can be induced, the vorticity vector must reorient, and the two extremities of the vortex filament must be perpendicular to the wall. These two ends gradually separate from each other as they convect downstream, as shown in Fig. 11. The distance between the propeller disk and point D (X_D) increases with increasing tip clearance or decreasing thrust coefficient. As this distance increases, the velocity deficit beneath the slipstream reduces until eventually the point of slipstream adherence to the wall disappears ($X_D \rightarrow \infty$), leaving a relatively undisturbed channel between the slipstream edge and the wall surface. This is reflected in Table 3, which provides the approximate location of point D for different thrust settings and tip clearances, based on additional PIV data.

V. Aerodynamic Interaction in the Presence of External Pressure Gradients

When the propeller is placed in close proximity to a flap, additional pressure gradients are generated due to the curvature of the surface, which affect the aerodynamic coupling between the two components. To analyze this interaction, the impact of the propeller on the flowfield over the flap is described in Sec. V.A. The influence of propeller

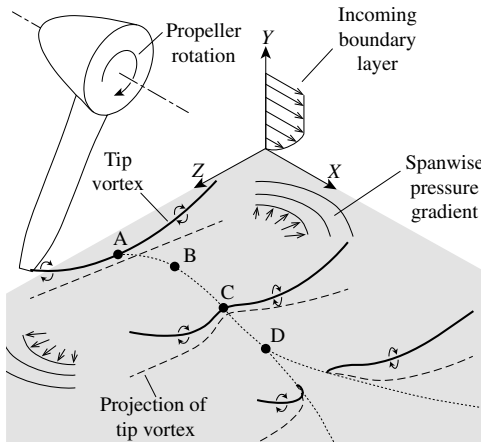


Fig. 16 Notional interpretation of the evolution of the tip vortices. The dotted line represents the trajectory of the lowest point of the vortex filament.

Table 3 Approximate location of point D (see Fig. 16), for different thrust settings and tip clearances

Constant thrust ($C_T = 0.35$)		Constant clearance ($\epsilon/R = 0.037$)	
ϵ/R	X_D/R	C_T	X_D/R
0.037	0.6	0.35	0.6
0.07	1.5	0.20	0.8
0.15	∞	0.10	∞

position is then addressed in Sec. V.B. Again, the results are presented for high thrust and low tip clearance ($BL_1, V_\infty = 20$ m/s, $C_T = 0.35$, and $\epsilon/R = 0.037$), unless explicitly mentioned otherwise. However, since the increased velocity over the flap surface decreases propeller thrust (see Fig. A2 of the Appendix), the rotational speed has to be increased to match the thrust coefficient C_T .

A. Propeller-Induced Flow Separation

When the flap is deflected, the velocity over the flap hinge is increased, as shown in Fig. 17a. The boundary-layer thickness grows considerably over the flap surface, although no flow reversal is observed in the FOV. However, Fig. 17b shows that, when the propeller is installed and operated at a high thrust setting, the axial momentum of the flow is increased and the flow separates over the flap. This indicates that the boundary layer cannot sustain the suction peak required on the flap surface to deflect the slipstream downward, and leads to a region of reverse flow, which is delimited by the white contour line. This also confirms that, in high-lift conditions, an over-the-wing propeller can cause flow separation, as identified in previous over-the-wing configuration studies [25].

Due to the propeller-induced flow separation, the propeller slipstream does not follow the flap surface. This is visible in the flowfield shown in Fig. 18. Although Fig. 18 presents the phase-averaged velocity distribution for $\phi = 5$ deg, the $\tilde{u}/V_\infty = 0$ boundary is representative of the ensemble-averaged distribution. This was concluded by comparing the velocity fields in the $Z/R = 0$ plane for

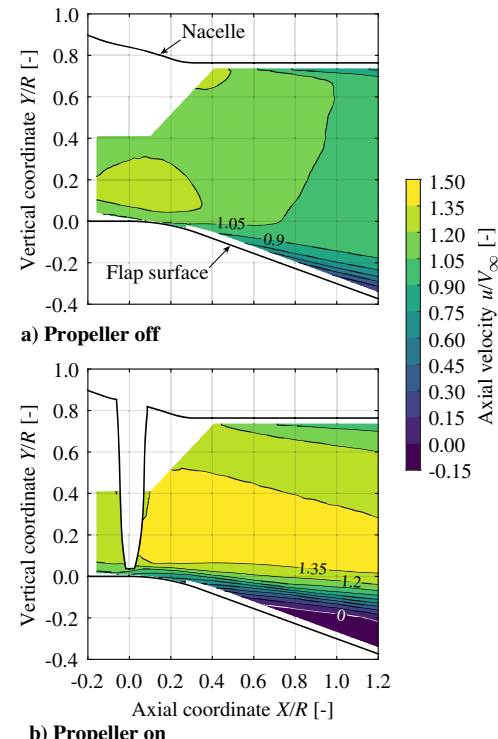


Fig. 17 Time-averaged axial-velocity distribution and streamlines between the nacelle and the flap surface.

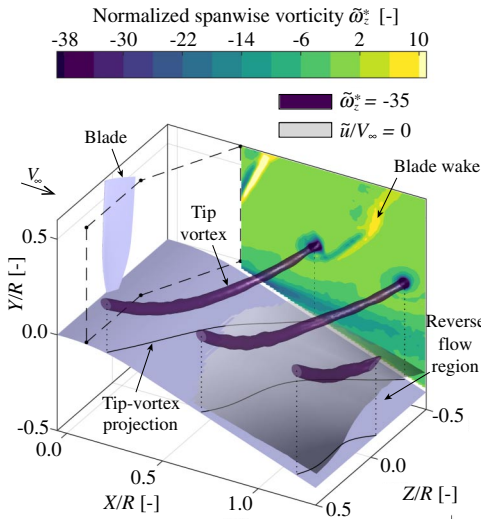


Fig. 18 Phase-averaged vorticity distribution downstream of propeller with flap deflected, including an axial-velocity isosurface that delimits the region of reverse flow ($\phi = 5$ deg, $e/R = 0.07$). Data only shown downstream of plane indicated by dashed lines.

different phase angles, which showed that the amount of flow reversal did not change significantly from one phase angle to another. Therefore, the severity of the propeller-induced flow separation is governed by the time-averaged influence of the propeller, and not by the periodic excitation of discrete tip vortices. This is a consequence of the relatively high excitation frequency when compared to a typical shedding frequency expected from the wing.¹¹

In this configuration, the tip vortices do not remain immersed in the wing boundary-layer (contrary to the flat-wall case), and hence they deform only slightly, without splitting into two. This is also visible in the propeller-induced surface-pressure fluctuations, shown in Fig. 19. The strong pressure fluctuations generated by the bound vorticity on the propeller blades are still visible beneath the propeller. However, the pressure fluctuations induced further downstream by the trailing vorticity in the slipstream have decreased considerably. Consequently, the "V"-shaped pattern (Fig. 11) is no longer present, although weak pressure fluctuations are still visible downstream of the propeller disk in Fig. 19. An analysis of the pressure spectra, not included here, showed that the pressure fluctuations downstream of the propeller ($X/R > 1$) contained only weak tonal components and a relatively strong broadband component. Therefore, the patches of increased fluctuations in this area are not created by flow structures in the slipstream, but by unsteady flow behavior in the separated-flow region. These pressure fluctuations are more prominent in the upper-right quadrant of Fig. 19, indicating that there is a slight asymmetry in the reverse-flow region. This is also reflected in Fig. 18, where the most upstream point of the \tilde{u}/V_∞ isosurface is located on the starboard side ($Z/R < 0$) of the center plane. The cause of this minor asymmetry could not be confirmed with the data available.

B. Impact of Propeller Position

Finally, this section describes how the propeller-induced flow separation is affected by the position of the propeller. To this end, Fig. 20 presents the phased-locked vorticity fields for three different configurations: the baseline configuration discussed in the previous section, a configuration with increased tip clearance, and a configuration where the propeller has been moved upstream by $0.05c$ while maintaining a constant tip clearance. The figure also includes the propeller-induced velocity vectors, which indicate the difference between the velocity field with the propeller on and the one obtained

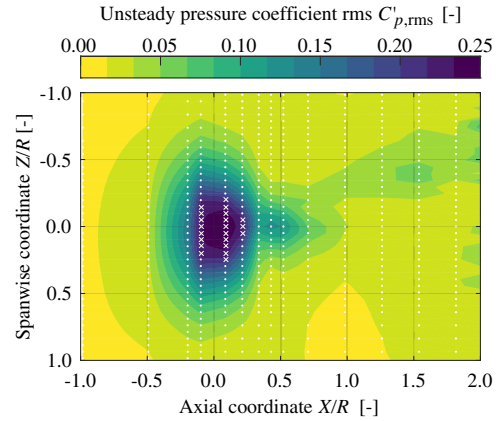


Fig. 19 Unsteady pressure-coefficient rms contours on the wing surface with flap deflection. Dots indicate measurement locations, whereas crosses indicate locations where maximum input level of microphone was exceeded.

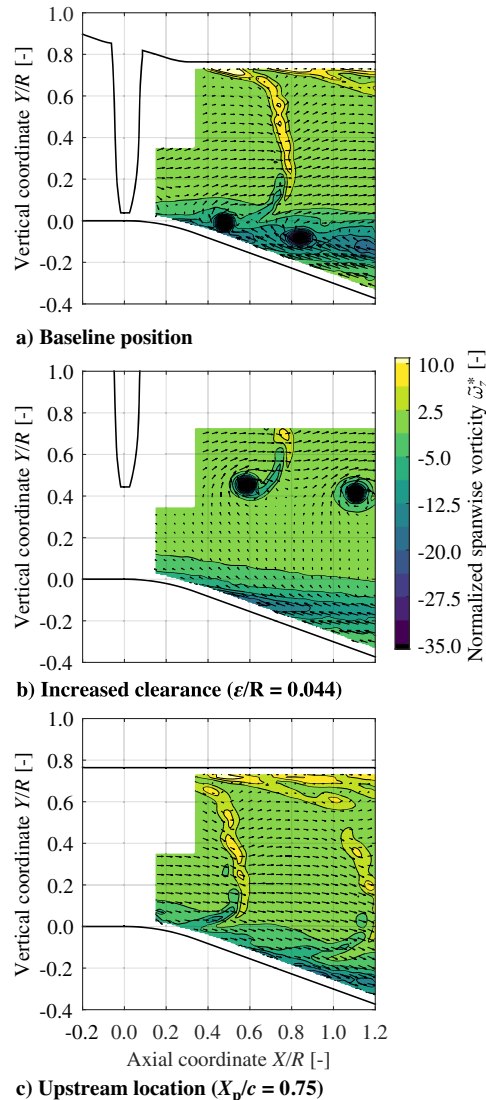


Fig. 20 Phase-averaged spanwise vorticity distribution and in-plane propeller-induced velocity vectors for three propeller positions.

¹¹Assuming a Strouhal number of 0.2, the natural shedding frequency would be around 45 Hz for a cylinder with a diameter equal to the thickness of the wing at the point of separation for the operating conditions considered, whereas the blade passage frequency is 531 Hz.

without the propeller. In the baseline configuration (Fig. 20a), the velocity vectors show how the velocity over the flap is significantly reduced, leading to the reverse-flow region shown in Fig. 17b. The region of strong (negative) vorticity around $Y/R = -0.1$ indicates the edge of the reverse-flow region, where a strong shear layer exists.

1. Effect of Propeller Tip Clearance

When the tip clearance is increased to $\epsilon/R = 0.44$, the velocity over the flap surface is still reduced with respect to propeller-off conditions, as shown in Fig. 20b. The shear line is also detached from the surface, indicating that the boundary layer has separated. Therefore, even though the blade tips are outside the boundary layer ($\epsilon = 3\delta_{99}$), the propeller still causes flow separation. This occurs because the high-momentum slipstream acts as a boundary, and a divergent flow channel is created between the slipstream edge and the flap surface. The divergent flow channel increases the adverse pressure gradient and causes the flow to separate. This confirms that, for these test conditions and geometry, the time-averaged effect of the propeller is the dominant cause for flow separation, and not the periodic excitation caused by the tip vortices. An inspection of the flowfields obtained with other tip clearances (Table 2), not included here, showed a similar effect. Increasing the tip clearance is therefore not an effective strategy to avoid propeller-induced flow separation.

2. Effect of Axial Position Relative to the Flap Hinge

Figure 20c shows how the flowfield is affected by placing the propeller further upstream. In this case, the velocity over the flap is increased with respect to propeller-off conditions, and the slipstream is locally parallel to the flap surface. Moreover, the tip vortices are not visible in the field of view. For this configuration, the boundary layer has slightly different thickness at the propeller location. However, this difference should play only a minor role since the boundary-layer thickness does not significantly affect the propeller thrust or the pressure gradient generated on the wing surface, as discussed previously. The differences with respect to the baseline configuration can therefore be explained by referring to the findings of Sec. IV. In the baseline configuration, the flap curvature starts directly beneath the propeller disk. The axial-velocity distribution in the flat-wall configuration (Fig. 6b) showed that, at that location, the slipstream contraction leads to a region of reduced axial velocity at the wall surface. The associated adverse pressure gradient is the dominant trigger for flow separation in the baseline flap-deflected configuration. However, further downstream of the propeller, the slipstream approaches the wall in the flat-wall configuration. This leads to a fuller boundary-layer profile with high-momentum flow near the surface (Fig. 6), and causes the tip vortices to split and move away from the $Z/R = 0$ plane (Fig. 15). Therefore, when the flap is deflected half a radius ($0.05c \approx 0.5R$) downstream of the propeller, the boundary layer is able to withstand strong adverse pressure gradients, and the flow remains attached. Consequently, the suction on the flap surface generates a Coandă effect [48,49], exerting a vertical force on the fluid and deflecting the high-momentum flow in the slipstream downward along the flap. This Coandă effect leads to an increase in system lift. Moreover, even though the tip vortices are not the dominant cause for flow separation, their absence from the flowfield in the $Z/R = 0$ region is beneficial for the boundary layer and further contributes to an attached flow over the flap.

VI. Conclusions

An experimental investigation has been performed to study the aerodynamic interaction between an over-the-wing propeller and the wing boundary layer. This interaction affects the separation of the boundary layer, and therefore has an important impact on the maximum lift coefficient attainable with OTW systems. To understand the underlying flow phenomena, first, the time-averaged impact of a propeller placed in close proximity to a flat wall is analyzed. Results show that a strong adverse pressure gradient is generated below the propeller disk, which increases linearly with thrust, decreases with increasing tip clearance, and is practically independent of the boundary-layer thickness. The associated contraction of the slipstream generates a region of reduced axial velocity between the slipstream edge and the wall. This region of reduced velocity extends approximately half a radius downstream of the propeller disk, beyond which the slipstream adheres to the wall and the thickness of the boundary layer is significantly reduced. An analysis of the

unsteady flowfield shows that the viscous interaction between the tip vortices and the boundary layer does not directly contribute to the downward displacement of the slipstream. However, the presence of the boundary layer deforms the tip vortices, causing them to self-induce a vertical velocity component and approach the wall. Each vortex filament then splits into two halves, which are convected downstream and induce pressure fluctuations on the wing surface in a characteristic V shape. The magnitude of these fluctuations is significantly lower than the ones created by the rotating blades' static-pressure fields, but still exceeds the time-averaged changes in surface pressure.

When the propeller operates at a high thrust setting above the flap hinge and an adverse pressure gradient is imposed by deflecting the flap, the flow can separate from the flap surface for two reasons. First, the strong adverse pressure gradient created beneath the propeller weakens the boundary layer (steady effect). Second, the periodic presence of the tip vortices leads to local axial-velocity deficits and pressure perturbations in the boundary layer, further reducing its capability to withstand an adverse pressure gradient (unsteady effect). A comparison of different flowfields shows that the former (steady effect) is the dominant cause for propeller-induced flow separation, whereas the unsteady effects play only a minor role. Additionally, an evaluation of different propeller positions indicates that increasing the tip clearance is not an effective mitigation strategy. However, if the propeller is placed half a radius upstream of the flap hinge, the boundary layer attains a fuller velocity profile over the flap, due to the downward displacement of the slipstream. This generates a Coandă effect, which allows the flow to remain attached and increase system lift when compared to propeller-off conditions.

These findings illustrate that the high-lift performance of over-the-wing propellers is very sensitive to the design of the system, and that a careful design is not possible without high-fidelity aerodynamic analyses. Besides, the Coandă effect observed in this study also confirms the potential of over-the-wing propellers to increase system lift. To maximize this performance benefit, the effect of propeller position and flap-deflection angle on the maximum lift coefficient of the system should be investigated using a more optimal wing shape. Since a more upstream placement of the propeller leads to a decrease in cruise performance, the propeller position can be maintained, and the flap size can be reduced by placing the flap hinge further aft, without compromising the maximum lift coefficient of the system. Alternative strategies to mitigate the propeller-induced flow separation should also be explored, such as a local adaptation of the wing profile, deflecting the propeller with the flap, or incorporating a secondary wing or duct to redirect the flow. Detailed aerodynamic analyses of such configurations are required to maximize the potential of distributed-propulsion systems, and therewith improve the overall efficiency of novel aircraft configurations.

Appendix: Propeller Performance

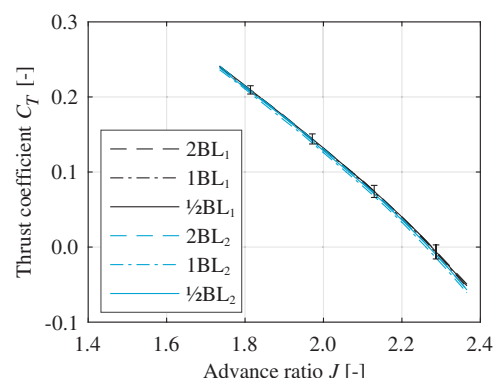


Fig. A1 Propeller thrust curves measured for different tip clearances and boundary-layer thicknesses in the flat-wall configuration ($V_\infty = 40$ m/s).

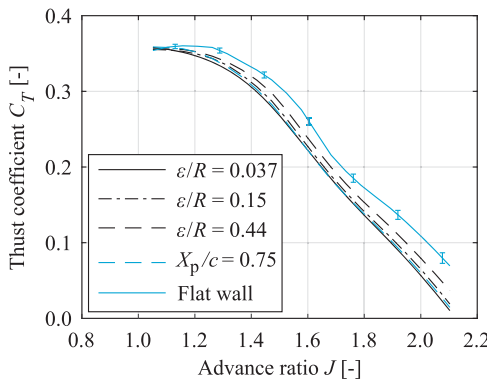


Fig. A2 Propeller thrust curves measured for $\delta_f = 20$ deg, $e/R = 0.037$, and $X_p/c = 0.8$, unless otherwise specified by the legend ($BL_1, V_\infty = 20$ m/s).

Acknowledgments

This research is funded by the European Union's Horizon 2020 Clean Sky 2 Large Passenger Aircraft program (CS2-LPA-GAM-2018-2019-01). The authors would like to thank Sören Bölk, Tomas Sinnige, and Biagio Della Corte for their help with the wind-tunnel experiments. The authors would also like to thank Jan Lisberg Jacobsen and Elrick L. Cornelius for providing the Sonion microphones.

References

- [1] Bonet, J. T., Schellenger, H. G., Rawdon, B. K., Elmer, K. R., Wakayama, S. R., Brown, D. L., and Guo, Y., "Environmentally Responsible Aviation (ERA) Project—N+2 Advanced Vehicle Concepts Study and Conceptual Design of Subscale Test Vehicle (STV): Final Report," NASA CR-2011-216519, Dec. 2011.
- [2] Anon., "Realising Europe's Vision for Aviation: Strategic Research & Innovation Agenda, Vol. 1," *Advisory Council for Aviation Research and Innovation in Europe*, 2012.
- [3] Felder, J. L., Brown, G. V., Kim, H. D., and Chu, J., "Turboelectric Distributed Propulsion in a Hybrid Wing Body Aircraft," *20th International Society for Airbreathing Engines (ISABE) Conference*, ISABE Paper 2011-1340, Sept. 2011.
- [4] Isikveren, A. T., Seitz, A., Bijewitz, J., Mirzoyan, A., Isyanov, A., Grenon, R., Atinault, O., Godard, J. L., and Stückl, S., "Distributed Propulsion and Ultra-High By-Pass Rotor Study at Aircraft Level," *Aeronautical Journal*, Vol. 119, No. 1221, 2015, pp. 1327–1376. <https://doi.org/10.1017/S0001924000011295>
- [5] Voskuilj, M., van Bogaert, J., and Rao, A. G., "Analysis and Design of Hybrid Electric Regional Turboprop Aircraft," *CEAS Aeronautical Journal*, Vol. 9, No. 1, 2018, pp. 15–25. <https://doi.org/10.1007/s13272-017-0272-1>
- [6] Schmollgruber, P., Donnat, D., Ridel, M., Cafarelli, I., Atinault, O., François, C., and Paluch, B., "Multidisciplinary Design and Performance of the ONERA Hybrid Electric Distributed Propulsion Concept (DRAGON)," *AIAA SciTech 2020 Forum*, AIAA Paper 2020-0501, Jan. 2020. <https://doi.org/10.2514/6.2020-0501>
- [7] Kim, H. D., "Distributed Propulsion Vehicles," *27th Congress of the International Council of the Aeronautical Sciences*, ICAS Paper 2010-1.1.3, Sept. 2010.
- [8] Borer, N. K., Patterson, M. D., Viken, J. K., Moore, M. D., Clarke, S., Redifer, M. E., Christie, R. J., Stoll, A. M., Dubois, A., Bevirt, J. B., Gibson, A. R., Foster, T. J., and Osterkamp, P. G., "Design and Performance of the NASA SCEPTOR Distributed Electric Propulsion Flight Demonstrator," *16th AIAA Aviation Technology, Integration, and Operations Conference*, AIAA Paper 2016-3920, June 2016. <https://doi.org/10.2514/6.2016-3920>
- [9] Müller, L., Heinze, W., Kožulović, D., Hepperle, M., and Radespiel, R., "Aerodynamic Installation Effects of an Over-the-Wing Propeller on a High-Lift Configuration," *Journal of Aircraft*, Vol. 51, No. 1, 2014, pp. 249–258. <https://doi.org/10.2514/1.C032307>
- [10] Johnson, J. L., Jr., and White, E. R., "Exploratory Low-Speed Wind-Tunnel Investigation of Advanced Commuter Configurations Including an Over-the-Wing Propeller," *AIAA Aircraft Design, Systems and Technology Meeting*, AIAA Paper 1983-2531, Oct. 1983. <https://doi.org/10.2514/6.1983-2531>
- [11] Cooper, R. K., McCann, W. J., and Chapleo, A. Q., "Over Wing Propeller Aerodynamics," *Proceedings of the 18th Congress of the International Council of the Aeronautical Sciences*, Vol. 18, AIAA, Washington, D.C., Sept. 1992, pp. 266–273.
- [12] Wang, K., Zhu, X. P., and Zhou, Z., "Numerical Simulation of the Propeller/Wing Interactions at Low Reynolds Number," *30th ICAS Congress*, ICAS Paper 2016-0075, Sept. 2016.
- [13] Broadbent, E. G., "Noise Shielding for Aircraft," *Progress in Aerospace Sciences*, Vol. 17, Jan. 1976, pp. 231–268. [https://doi.org/10.1016/0376-0421\(76\)90009-9](https://doi.org/10.1016/0376-0421(76)90009-9)
- [14] Beck, S. C., Müller, L., and Langer, S. C., "Numerical Assessment of the Vibration Control Effects of Porous Liners on an Over-the-Wing Propeller Configuration," *CEAS Aeronautical Journal*, Vol. 7, No. 2, 2016, pp. 275–286. <https://doi.org/10.1007/s13272-016-0186-3>
- [15] Wang, H., Gan, W., and Li, D., "An Investigation of the Aerodynamic Performance for a Fuel Saving Double Channel Wing Configuration," *Energies*, Vol. 12, No. 20, 2019, pp. 1–16. <https://doi.org/10.3390/en12203911>
- [16] Veldhuis, L. L. M., "Propeller Wing Aerodynamic Interference," Ph.D. Dissertation, Delft Univ. of Technology, Delft, The Netherlands, 2005.
- [17] de Vries, R., Hoogreef, M. F. M., and Vos, R., "Preliminary Sizing of a Hybrid-Electric Passenger Aircraft Featuring Over-the-Wing Distributed-Propulsion," *AIAA SciTech 2019 Forum*, AIAA Paper 2019-1811, Jan. 2019. <https://doi.org/10.2514/6.2019-1811>
- [18] Marcus, E. A. P., de Vries, R., Raju Kulkarni, A., and Veldhuis, L. L. M., "Aerodynamic Investigation of an Over-the-Wing Propeller for Distributed Propulsion," *2018 AIAA Aerospace Sciences Meeting*, AIAA Paper 2018-2053, Jan. 2018. <https://doi.org/10.2514/6.2018-2053>
- [19] Ma, Y., Zhang, W., Zhang, Y., Zhang, X., and Zhong, Y., "Sizing Method and Sensitivity Analysis for Distributed Electric Propulsion Aircraft," *Journal of Aircraft*, Vol. 57, No. 4, 2020, pp. 730–741. <https://doi.org/10.2514/1.C035581>
- [20] Perry, A. T., Ansell, P. J., and Kerho, M. F., "Aero-Propulsive and Propulsor Cross-Coupling Effects on a Distributed Propulsion System," *Journal of Aircraft*, Vol. 55, No. 6, 2018, pp. 2414–2426. <https://doi.org/10.2514/1.C034861>
- [21] Upadhyay, P., and Zaman, K. B. M. Q., "The Effect of Incoming Boundary Layer Characteristics on the Performance of a Distributed Propulsion System," *AIAA SciTech 2019 Forum*, AIAA Paper 2019-1092, Jan. 2019. <https://doi.org/10.2514/6.2019-1092>
- [22] Hermetz, J., Ridel, M., and Döll, C., "Distributed Electric Propulsion for Small Business Aircraft: A Concept-Plane for Key-Technologies Investigations," *30th ICAS Congress*, ICAS Paper 2016-0461, Sept. 2016.
- [23] Müller, L., Kožulović, D., and Radespiel, R., "Aerodynamic Performance of an Over-the-Wing Propeller Configuration at Increasing Mach Number," *CEAS Aeronautical Journal*, Vol. 5, No. 3, 2014, pp. 305–317. <https://doi.org/10.1007/s13272-014-0108-1>
- [24] de Vries, R., Brown, M., and Vos, R., "Preliminary Sizing Method for Hybrid-Electric Distributed-Propulsion Aircraft," *Journal of Aircraft*, Vol. 56, No. 6, 2019, pp. 2172–2188. <https://doi.org/10.2514/1.C035388>
- [25] Müller, L., Friedrichs, J., and Kožulović, D., "Unsteady Flow Simulations of an Over-the-Wing Propeller Configuration," *50th AIAA/ASME/SAE/ASEE Joint Propulsion Conference*, AIAA Paper 2014-3886, July 2014. <https://doi.org/10.2514/6.2014-3886>
- [26] Peridier, V. J., Smith, F. T., and Walker, J. D. A., "Vortex-Induced Boundary-Layer Separation. Part 2. Unsteady Interacting Boundary-Layer Theory," *Journal of Fluid Mechanics*, Vol. 232, Nov. 1991, pp. 133–165. <https://doi.org/10.1017/S0022112091003658>
- [27] Sengupta, T. K., De, S., and Sarkar, S., "Vortex-Induced Instability of an Incompressible Wall-Bounded Shear Layer," *Journal of Fluid Mechanics*, Vol. 493, Oct. 2003, pp. 277–286. <https://doi.org/10.1017/S0022112003005822>
- [28] Dolicinski, T. L., Smith, C. R., and Walker, J. D. A., "Vortex Interactions with Walls," *Annual Review of Fluid Mechanics*, Vol. 26, No. 1, 1994, pp. 573–616. <https://doi.org/10.1146/annurev.fl.26.010194.003041>
- [29] Chuang, F.-S., and Conlisk, A. T., "The Effect of Interaction on the Boundary Layer Induced by a Convected Rectilinear Vortex," *Journal of Fluid Mechanics*, Vol. 200, March 1989, pp. 337–365. <https://doi.org/10.1017/S0022112089000686>

- [30] Straus, J., and Mayle, R. E., "Boundary-Layer Measurements During a Parallel Blade-Vortex Interaction," *10th Applied Aerodynamics Conference*, AIAA Paper 1992-2623, June 1992.
<https://doi.org/10.2514/6.1992-2623>
- [31] Doligalski, T. L., and Walker, J. D. A., "The Boundary Layer Induced by a Convected Two-Dimensional Vortex," *Journal of Fluid Mechanics*, Vol. 139, Feb. 1984, pp. 1–28.
<https://doi.org/10.1017/S0022112084000240>
- [32] Murray, H. H., IV, Devenport, W. J., Alexander, W. N., Glegg, S. A. L., and Wida, D., "Aeroacoustics of a Rotor Ingesting a Planar Boundary Layer at High Thrust," *Journal of Fluid Mechanics*, Vol. 850, Sept. 2018, pp. 212–245.
<https://doi.org/10.1017/jfm.2018.438>
- [33] Yang, Y., Sciacchitano, A., Veldhuis, L. L. M., and Eitelberg, G., "Analysis of Propeller-Induced Ground Vortices by Particle Image Velocimetry," *Journal of Visualization*, Vol. 21, No. 1, 2018, pp. 39–55.
<https://doi.org/10.1007/s12650-017-0439-1>
- [34] Martio, J., Sipilä, T., Sanchez-Caja, A., Saisto, I., and Siikonen, T., "Evaluation of the Propeller Hull Vortex Using a RANS Solver," *Second International Symposium on Marine Propulsors*, Paper TB1-3, June 2011.
- [35] Sato, R., Tasaki, R., and Nishiyama, S., "Observation of Flow on a Horizontal Flat Plate Above a Working Propeller and Physics of Propeller-Hull Vortex Cavitation," *Proceedings of the International Symposium on Propeller and Cavitation*, China International Book Trading Corporation, Beijing, China, April 1986, pp. 118–125.
- [36] Williams, M. H., Cho, J., and Dalton, W. N., "Unsteady Aerodynamic Analysis of Ducted Fans," *Journal of Propulsion and Power*, Vol. 7, No. 5, 1991, pp. 800–804.
<https://doi.org/10.2514/3.23394>
- [37] Bento, H. F. M., de Vries, R., and Veldhuis, L. L. M., "Aerodynamic Performance and Interaction Effects of Circular and Square Ducted Propellers," *AIAA SciTech 2020 Forum*, AIAA Paper 2020-1029, Jan. 2020.
<https://doi.org/10.2514/6.2020-1029>
- [38] Avallone, F., Ragni, D., and Casalino, D., "On the Effect of the Tip-Clearance Ratio on the Aeroacoustics of a Diffuser-Augmented Wind Turbine," *Renewable Energy*, Vol. 152, June 2020, pp. 1317–1327.
<https://doi.org/10.1016/j.renene.2020.01.064>
- [39] Lin, N., Reed, H. L., and Saric, W. S., "Effect of Leading-Edge Geometry on Boundary-Layer Receptivity to Freestream Sound," *Instability, Transition, and Turbulence*, Springer, New York, 1992, pp. 421–440.
https://doi.org/10.1007/978-1-4612-2956-8_42
- [40] Li, Q., Öztürk, K., Sinnige, T., Ragni, D., Eitelberg, G., Veldhuis, L. L. M., and Wang, Y., "Design and Experimental Validation of Swirl-Recovery Vanes for Propeller Propulsion Systems," *AIAA Journal*, Vol. 56, No. 12, 2018, pp. 4719–4729.
<https://doi.org/10.2514/1.J057113>
- [41] van Arnhem, N., de Vries, R., Sinnige, T., Vos, R., Eitelberg, G., and Veldhuis, L. L. M., "Engineering Method to Estimate the Blade Loading of Propellers in Nonuniform Flow," *AIAA Journal*, Vol. 58, No. 11, 2020, pp. 1–15.
<https://doi.org/10.2514/1.J059485>
- [42] Ewald, B. F. R., "Wind Tunnel Wall Corrections (la Correction des Effets de Paroi en Soufflerie)," Advisory Group for Aerospace Research and Development Rept. AGARD-AG-336, Neuilly-Sur-Seine, France, 1998.
- [43] Schlichting, H., *Boundary-Layer Theory*, 7th ed., McGraw-Hill, New York, 1979, pp. 635–647, Chap. XXI.
<https://doi.org/10.1007/978-3-662-52919-5>
- [44] Yang, Y., "Aerodynamic Interaction Between Propeller and Vortex," Ph.D. Dissertation, Delft Univ. of Technology, Delft, The Netherlands, 2017.
- [45] Durand, W. F., *Aerodynamic Theory*, Vol. II, Julius Springer, Berlin, 1935, pp. 367–369, Div. M, Chap. 1.
<https://doi.org/10.1007/978-3-662-39765-7>
- [46] Sinnige, T., de Vries, R., Della Corte, B., Avallone, F., Ragni, D., Eitelberg, G., and Veldhuis, L. L. M., "Unsteady Pylon Loading Caused by Propeller-Slipstream Impingement for Tip-Mounted Propellers," *Journal of Aircraft*, Vol. 55, No. 4, 2018, pp. 1605–1618.
<https://doi.org/10.2514/1.C034696>
- [47] Levy, H., and Forsdyke, A. G., "The Steady Motion and Stability of a Helical Vortex," *Proceedings of the Royal Society of London, Series A: Mathematical and Physical Sciences*, Vol. 120, No. 786, 1928, pp. 670–690.
<https://doi.org/10.1098/rspa.1928.0174>
- [48] Wille, R., and Fernholz, H., "Report on the First European Mechanics Colloquium, on the Coanda Effect," *Journal of Fluid Mechanics*, Vol. 23, No. 4, 1965, pp. 801–819.
<https://doi.org/10.1017/S0022112065001702>
- [49] Reba, I., "Applications of the Coanda Effect," *Scientific American*, Vol. 214, No. 6, 1966, pp. 84–92.
<https://doi.org/10.1038/scientificamerican0666-84>

A. R. Jones
Associate Editor